

**Pipeline flotation in liquefied sand
A simplified transient model**

Pisanò, F.; Betto, D.; Della Vecchia, G.; Cremonesi, M.

DOI

[10.1016/j.oceaneng.2022.113146](https://doi.org/10.1016/j.oceaneng.2022.113146)

Publication date

2022

Document Version

Final published version

Published in

Ocean Engineering

Citation (APA)

Pisanò, F., Betto, D., Della Vecchia, G., & Cremonesi, M. (2022). Pipeline flotation in liquefied sand: A simplified transient model. *Ocean Engineering*, 266, Article 113146. <https://doi.org/10.1016/j.oceaneng.2022.113146>

Important note

To cite this publication, please use the final published version (if applicable). Please check the document version above.

Copyright

Other than for strictly personal use, it is not permitted to download, forward or distribute the text or part of it, without the consent of the author(s) and/or copyright holder(s), unless the work is under an open content license such as Creative Commons.

Takedown policy

Please contact us and provide details if you believe this document breaches copyrights. We will remove access to the work immediately and investigate your claim.



Pipeline flotation in liquefied sand: A simplified transient model

F. Pisanò^{a,*}, D. Betto^b, G. Della Vecchia^b, M. Cremonesi^b

^a Faculty of Civil Engineering and Geosciences, Delft University of Technology, Stevinweg 1, Delft, 2628 CN, The Netherlands

^b Department of Civil and Environmental Engineering, Politecnico di Milano, piazza L. da Vinci 32, Milano, 20133, Italy

ARTICLE INFO

Keywords:

Submarine pipelines
Flotation
Sand liquefaction
Bingham rheology
Soil consolidation

ABSTRACT

Submarine buried pipelines are often laid in trenches backfilled with loose sandy soil, which is intrinsically prone to liquefaction. When liquefaction is triggered, the soil tends to behave as a viscous fluid with vanishing shear strength and very limited ability to restrain structural displacement, for instance during the occurrence of pipeline flotation. Recently, a 2D CFD-based approach for the analysis of pipe flotation in liquefied sand has been proposed by Pisano et al. (2020), in which soil reconsolidation effects are phenomenologically captured by considering rheological parameters that evolve in space and time as pore water pressures dissipate. Despite a remarkable agreement with experimental data from the literature, the complexity and computational costs of such approach may still hinder its applicability to pipeline engineering practice. To overcome this limitation, a simplified model is proposed herein, in which all the forces governing the motion of the pipe are expressed via simple analytical relationships. After thorough validation against 2D CFD results and relevant experimental data, it is concluded that the new simplified model largely retains the predictive capability of Pisano et al.'s framework in combination with negligible computational costs.

1. Introduction

Approximately a quarter of the present oil and gas supply is produced offshore, mostly in the Middle East, the North Sea, Brazil, the Gulf of Mexico and the Caspian Sea. The recent projections of the International Energy Agency highlight that, up until 2040, the amount of hydrocarbon-related offshore activities will continue to increase (IEA, 2018). In this context, pipelines will continue to play a crucial role in enabling the transport of hydrocarbons from wells to in-field processing facilities and finally to shore.

When directly laid on the seabed, pipelines are often exposed to harsh hydrodynamic loads that may negatively impact their structural performance. Although pipelines can usually withstand large displacements, a stabilisation measure is often employed. A typical stabilisation option is to lay pipelines in trenches backfilled with rocks or sand. Pipe trenching can be very expensive, but it can increase the lateral resistance and drastically reduce hydrodynamic forces (Teh et al., 2006; Bai and Bai, 2014).

Pipelines buried in uncompacted sandy backfill may suffer from the consequences of soil liquefaction, possibly induced by structural vibrations, ocean waves, tidal fluctuations, or earthquakes (Sumer et al., 1999; de Groot et al., 2006; Luan et al., 2008). The occurrence of liquefaction is generally associated with the loose state of the backfill under the low effective stresses at shallow soil depth — though with an influence of the previous stress/strain history (Finn et al., 1970;

Ishihara and Okada, 1978). Due to the low strength and stiffness of fluidised soils, segments of buried pipelines may experience excessive displacement, for instance in the form of vertical flotation or sinking. In the presence of relatively light pipelines, the large(r) unit weight of liquefied sand is often the main trigger of the flotation process, simply as a consequence of Archimedes' principle; other driving mechanisms are also possible, e.g., in the presence of a strong upward pore water pressure gradient or due to upheaval buckling (especially for high-temperature high-pressure pipelines) (Teh et al., 2006). After the first studies in the United States (Pipeline Flotation Research Council, 1966), North Sea offshore developments motivated further in-depth research regarding the impact of soil liquefaction on the stability of trenched pipelines (Sumer et al., 1999; Damgaard and Palmer, 2001). Relevant outcomes of these research efforts are presently reflected by relevant industry standards (DNV, 2021a,b,c).

Since pipeline routes may not always avoid liquefiable areas, geotechnical input to pipeline design must include the prediction of flotation-induced deformations whenever soil liquefaction risk is anticipated. In fact, vertical movement can lead to a limit state in which the structural security of the pipeline is compromised, either by excessive bending or by overloading of attached structures (e.g., other pipeline branches or wellheads). If flotation results in the resurfacing of (a segment of) the pipeline, then the effectiveness of trenching as a

* Corresponding author.

E-mail address: f.pisano@tudelft.nl (F. Pisanò).

stabilisation method may be jeopardised. In this respect, geometrical settings do naturally play a role, for instance depending on the ratio between pipeline diameter and embedment, as well as on the trench width. Tubes of diameter D from 0.25 m to 1.5 m are most often used in practice, in combination with values of embedment depth (b , thickness of the soil cover) and trench width (d , average value for a trapezoidal cross-section) such that $1.5 < b/D < 7$ for $D < 0.75$ m (small-diameter tubes) and $0.75 < b/D < 2$ for $D > 0.75$ m (medium/large-diameter tubes), and $1.5 < d/D < 7$.

Although some previous studies have already researched the uplift resistance of pipelines in loose liquefiable sand (Schupp et al., 2006; Byrne et al., 2013), there are to date no well-established methods for predicting pipeline displacement in relation to soil liquefaction phenomena. To fill this knowledge gap, Pisanò et al. (2020) proposed a novel approach based on Computational Fluid Dynamics (CFD), accounting for large deformations and possible reconsolidation effects in the soil. More specifically, the proposed approach idealises the fluidised backfill in the trench as a Non-Newtonian (Bingham) fluid, whereas the analysis of pipe-soil interaction during flotation is carried out, within a one-phase modelling framework, using the so-called Particle Finite Element Method (PFEM). As excess pore pressures in the soil may swiftly dissipate, it has been shown how a phenomenological update – both in space and time – of evolving rheological properties can enable successful simulation of liquefied sand's interaction with buried pipelines. This approach is consistent with available experimental evidence (Nishimura et al., 2002; Gallage et al., 2005; Guoxing et al., 2016), and allows the study of pipeline motion in reconsolidating soil without abandoning the reference fluid modelling framework.

It should be acknowledged, however, that Pisanò et al.'s approach requires the numerical solution of a complex fluid–structure interaction problem, which appears to be beyond the level of complexity that is normally acceptable for practical design calculations. To overcome these difficulties, this paper proposes a simplification of the original approach in the form of a ‘reduced’ model that can be easily implemented and utilised by practising engineers. The proposed simplified model introduces physics-based analytical relationships to describe the main forces affecting the motion of a floating pipe in liquefied – and possibly reconsolidating – sand, without resorting to demanding 2D/3D CFD simulations. The remainder of the paper is dedicated to the physical validation of the simplified model, both against complete 2D PFEM simulation results and small-scale experimental data from the literature. The twofold goal of this work is to cover the conceptual development of the model and prove its predictive capability after proper calibration. In the latter regard, existing uncertainties about the mechanical properties of liquefied sand are discussed in relation to the specific application at hand, in a fashion that preludes to further studies on the subject.

2. Simplified model formulation

Characterising the nature and state of the backfill material is key to assessing the stability of submarine buried pipelines. Trenches are usually backfilled with materials that are available on site; once laid in trench, these materials are frequently very loose and thus prone to liquefaction. If liquefaction does take place, then (segments of) the pipeline may undergo either flotation or sinking, which would negatively impact structural integrity.

Although pipeline networks are in reality three-dimensional, detailed stability studies on specific segments of the infrastructure are often tackled through two-dimensional approaches, focusing on the interaction between pipe cross-section and surrounding soil. In this context, a two-dimensional approach has been recently proposed by Pisanò et al. (2020) to simulate the evolution in time of the pipe upward displacement while the soil is initially fully liquefied and gradually reconsolidating. The model builds on an enhanced one-phase (total-stress) approach, in which the liquefied sand is modelled as a Bingham

fluid (see Eqs. (1a) and (1b)). In the simplest case of one-dimensional shear flow, the behaviour of a Bingham fluid is characterised by only two rheological parameters, namely the yield stress τ_y and the viscosity η :

$$\tau = \tau_y + \eta \dot{\gamma} \quad \text{if } \tau > \tau_y \quad (1a)$$

$$\dot{\gamma} = 0 \quad \text{otherwise} \quad (1b)$$

where τ and $\dot{\gamma}$ denote the shear stress and shear strain rate, respectively – the multi-axial generalisation of the Bingham model for 2D/3D flow is straightforward and provided, for instance, by Cremonesi et al. (2011). From a physical standpoint, τ_y denotes the shear stress threshold above which indefinite fluid flow may take place – and below which the fluid may only deform with a vanishing strain rate. On the other hand, the occurrence of unlimited deviatoric deformation beyond the material shear strength recalls the concept of failure as typically meant in solid mechanics. This observation leads to recognise, in the context of total stress analysis, a fundamental equivalence between τ_y and the so-called undrained shear strength s_u , which is commonly adopted as a geotechnical material parameter for the study of quasi-static failure problems. Regarding the case of liquefied sand, τ_y appears to be most closely related to the steady-state shear strength s_u , as defined by Poulos (1981) – see also discussion in Section 2.5.

The numerical solution of the interaction problem involving the buried pipe and the surrounding liquefied sand is carried out in Pisanò et al. (2020) using the PFEM developed by Cremonesi et al. (2010) after (Idelsohn et al., 2004). Accordingly, a fully Lagrangian description of the fluid flow is adopted, which is especially suitable for problems related to free-surface flow and fluid–structure interaction (Cremonesi et al., 2020). Despite their theoretical and computational soundness, however, CFD methods – including the PFEM – require the implementation of advanced numerical algorithms and specific expertise of the user (e.g., regarding the choice of space–time discretisation settings). This observation, along with the relatively high computational costs of PFEM simulations, have motivated the development of the simplified interaction model that is described in what follows.

Proposed herein is a model that tackles pipe–fluid interaction at a macro-element scale, i.e., by representing the pipe (cross-section) as a lumped point mass subjected to time-varying forces (Fig. 1). Only vertical components of force and displacement/velocity/acceleration are considered (y direction in Fig. 1(b)), which is sufficient for describing the upward motion of a circular rigid body. While moving through the fluidised soil, the pipe is subjected to three distinct external forces (per unit length), namely its self-weight (W), the buoyancy force (F_B), and the drag resistance (F_D). The sum of F_B and F_D equals the integral over the pipe section perimeter of the Cauchy stress distribution, which emerges from the interaction between pipe and surrounding fluid (Fig. 1(a)). When appropriate, a structural restoring force may be included to reproduce the connection of the considered pipe section with the rest of the pipeline network – see validation example in Section 4.1.

The flotation-induced displacement of the pipe, u , may be simply obtained by integrating in time the following dynamic equilibrium equation along the y direction:

$$m \ddot{u} = F_B - W - F_D(\dot{u}) \quad (2)$$

where m is the mass of the pipe per unit length, and \ddot{u} its vertical acceleration (dots are used to indicate time differentiation, while $F_D(\dot{u})$ denotes the dependence of F_D on \dot{u}). While the self-weight and the buoyancy force are always, respectively, downward- and upward-oriented, the direction of the drag force opposes the motion of the pipe – i.e., downward drag applies to the case of a floating pipe, as assumed in Eq. (2).

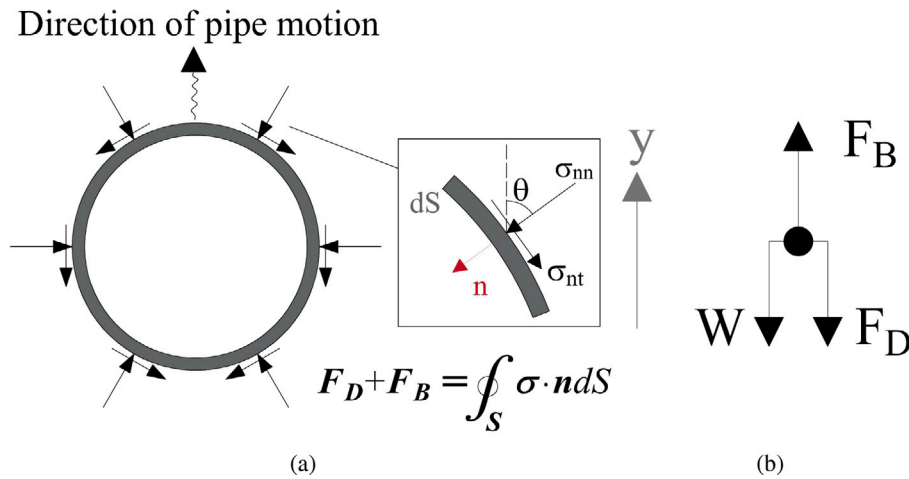


Fig. 1. (a) Fluid stress distribution over the pipe section perimeter and corresponding integral forces (σ is the Cauchy stress tensor, while σ_{nn} and σ_{nt} are the normal and tangential components of the traction vector, respectively); (b) force scheme for the simplified macro-element approach.

2.1. Self-weight and buoyancy

Submarine buried pipelines are generally used to carry hydrocarbons or other fluids. In the spirit of a macro-element approach, an equivalent density ρ_{eq} may be used to evaluate the self-weight of the pipe. The weight per unit length of a pipe of outer diameter D and wall thickness t is:

$$W = \rho_{eq} \frac{\pi D^2}{4} g \quad \text{with} \quad \rho_{eq} = [\rho_p \cdot D^2 + (\rho_f - \rho_p) \cdot (D - 2t)^2] / D^2 \quad (3)$$

where g is the gravitational acceleration and ρ_{eq} the equivalent density – with ρ_p and ρ_f being the mass density of the pipe and the flowing fluid, respectively. In agreement with relevant international standards (API, 2004; ISO, 2012), a ratio $D/t = 20$ is henceforth assumed; on the safe side with regard to flotation assessment, the case of an empty pipe is considered in this work (i.e., $\rho_f = 0$).

As for the evaluation of the buoyancy term, it should first be mentioned that significant uncertainties affect the estimation of liquefied sand’s density, ρ_{ls} . Based on previous experimental studies (Sumer et al., 2006; Teh et al., 2006), ρ_{ls} may lie in the range between 1800 and 2000 kg/m³. In order to reduce the number of free parameters for model calibration purposes, $\rho_{ls} = 1800$ kg/m³ is henceforth assumed, unless stated otherwise. It is thus straightforward to determine the buoyancy force per unit length as follows:

$$F_B = \rho_{ls} \frac{\pi D^2}{4} g \quad (4)$$

2.2. Drag force

When a body moves through a fluid mass – or is immersed within a flowing fluid – a drag force arises. A careful literature review has put in evidence the dearth of applicable research on the estimation of drag forces on floating cylinders, especially in comparison to the numerous studies that have been devoted to the case of fixed cylinders immersed in flow fields of different type. The latter kind of studies have been carried out by accounting for different rheological behaviours, both Newtonian (Oseen, 1910; Lamb, 1911; White, 1946; Tomotika and Aoi, 1951; Takaisi, 1956; Zdravkovich, 1979) and Non-Newtonian (Bingham) (Adachi and Yoshioka, 1973; De Besses et al., 2003; Mitsoulis, 2004; Tokpavi et al., 2008; Nirmalkar et al., 2012).

Unfortunately, available expressions for estimating the drag force experienced by an infinitely long cylinder immersed in a flowing Bingham fluid are not directly applicable to the flotation problem at hand as formulated in Eq. (2). Two main reasons hinder direct use of previous research findings: (i) the typical assumption of uniform/stationary flow does not apply to the velocity field around a floating pipe; (ii) most of

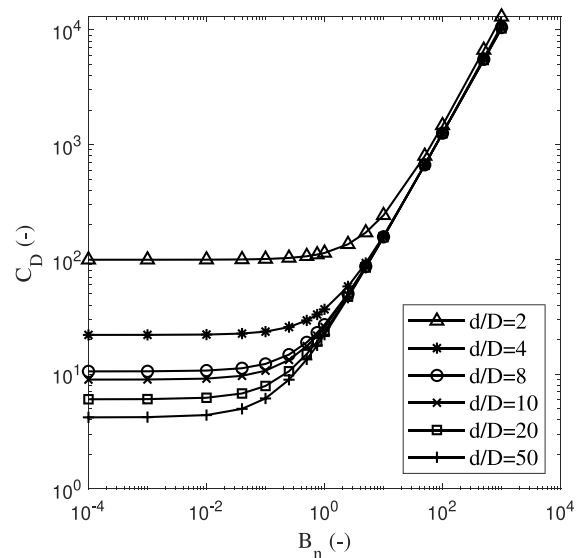


Fig. 2. Normalised drag force versus Bingham number for an infinitely long cylinder immersed in a Bingham fluid that flows uniformly between two planar boundaries. Different curves are associated with distinct values of the distance between boundaries – redrawn after Mitsoulis (2004).

the drag formulas from the literature neglect boundary effects, which may be relevant to pipe flotation in a relatively narrow trench.

Boundary effects are considered in the study of Mitsoulis (2004), who proposed an expression of the drag force F_D for infinitely long cylinders immersed in a Bingham fluid that flows uniformly between two planar rough boundaries at a distance equal to d . The relationship between the normalised drag force (C_D) and the Bingham number (B_n) according to Mitsoulis (2004) is shown in Fig. 2 for different d/D ratios, with the following meaning of the adopted symbols:

$$C_D = \frac{F_D}{\eta \dot{u}} \quad B_n = \frac{\tau_y D}{\eta \dot{u}} \quad (5)$$

where η and τ_y are the Bingham fluid parameters as in Eq. (1a), and \dot{u} the inflow velocity of the fluid. It is evident that for large values of B_n (i.e., when the ‘plastic drag’ prevails over the ‘viscous drag’) C_D is nearly unaffected by d/D , which implies negligible influence of the confining boundaries. Conversely, as lower B_n values are considered, the behaviour of a Newtonian fluid is approached, with dominant viscous drag and marked influence of the d/D ratio.

Building on the results in Fig. 2, an (approximate) additive decomposition of the drag force is assumed for the evaluation of F_D in Eq. (2):

$$F_D = F_{D,p} + F_{D,v} \quad (6)$$

where $F_{D,p}$ and $F_{D,v}$ represent, respectively, the ‘plastic’ and the ‘viscous’ contributions to the total drag force.

The plastic drag component, $F_{D,p}$ is directly related to the Bingham yield stress τ_y . The aforementioned equivalence between τ_y and s_u underlies the conceptual link between the plastic drag $F_{D,p}$ and the resisting force R_{uplift} that, under undrained quasi-static conditions, must be overcome for the uplift of a buried pipe (Bransby et al., 2002). R_{uplift} may be estimated using an equation of the following form:

$$R_{uplift} = N_b s_u D \quad (7)$$

where N_b is an uplift resistance factor that is traditionally obtained via plastic limit analysis calculations (Chen and Liu, 2012; Sloan, 2013). According to DNV (2021b), the N_b factor:

- (i) is associated with a local soil failure mechanism, where the soil above the pipe will displace around and below the pipe as the pipe moves upwards. For small embedment depths, R_{uplift} will be limited by the resistance associated with a global soil failure mechanism, i.e., with a failure surface extending up to the seabed — this specific case is not further investigated herein;
- (ii) is depth-dependent for shallow embedment, $0 < b/D < 4$, while for $b/D \geq 4$ it reaches a theoretical value N_c in the range between 9 (smooth pipe surface) and 12 (rough pipe surface) (Randolph and Houlsby, 1984);
- (iii) is also affected by physical mechanisms that are not captured by plastic limit analysis solutions, including time effects in real soil behaviour and progressive failure. To account for these aspects, DNV (2021b) recommends to obtain N_b as the product between N_c (plastic limit analysis solution) and an empirical factor in the range between 0.55 and 0.8, with a best estimate value of 0.65.

It is worth remarking that Eq. (7) only applies to quasi-static conditions, i.e., to the case of a very slowly moving pipe. More general dynamic conditions may be tackled by incorporating a direct dependence of the plastic drag force on the Bingham number:

$$F_{D,p} = C_{D,p}(B_n) \tau_y D \quad (8)$$

where the plastic drag coefficient, $C_{D,p}$, is explicitly a function of the Bingham number — the definition of B_n in Eq. (5) is adapted to flotation problems by setting \dot{u} as the (current) velocity of the moving pipe.

The viscous drag component, $F_{D,v}$, is dominant for low Bingham numbers and may be evaluated based on the work of White (1946), who proposed the following empirical relationship after studying the drag force acting on a wire falling through a Newtonian fluid between two vertical walls:

$$F_{D,v} = \frac{6.4 \eta \dot{u}}{\log\left(\frac{d}{D}\right)} \quad (9)$$

in which there is an obvious influence of boundary distance effects, even for d/D values as large as 500. It is worth noting that White’s formula is solely valid for the case of laminar flow, which seems appropriate for pipe flotation in a highly viscous fluid, such as liquefied sand.

Although this work focuses on vertical flotation, the experimental literature includes data from lateral pipe dragging tests, which have been here exploited to achieve broader validation of the proposed modelling framework — see Section 4.3. If the pipe moves horizontally across a fluid mass bounded by a bottom rigid plane, then the following

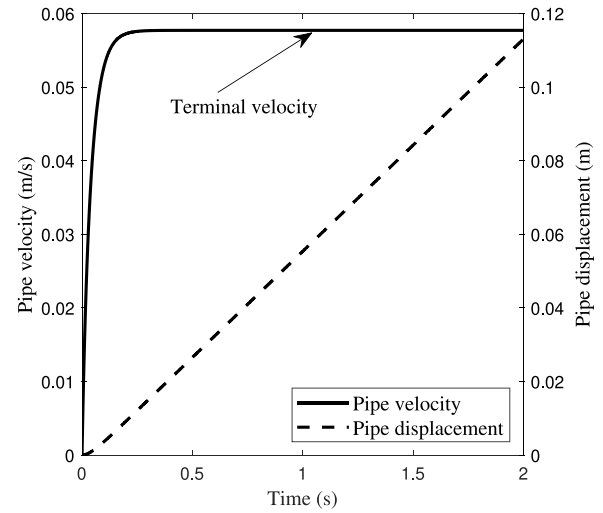


Fig. 3. Example of pipe motion scenario returned by the simplified model in combination with the following geometrical/mechanical parameters: $D = 0.8$ m, $d/D = 6$, $\rho_{ls} = 1800$ kg/m³, $\eta = 2000$ Pa·s, $\tau_y = 50$ Pa.

drag equation proposed by Takaisi (1956) will return more accurate results:

$$F_{D,v} = \frac{4\pi\eta\dot{u}}{\ln\left(\frac{2h_p+D}{D/2}\right) - \frac{1}{4}\left(\frac{D}{2h_p+D}\right)^2} \quad (10)$$

where h_p is the elevation of the pipe above the underlying rigid boundary – i.e., with the same meaning as sketched in Section 4.1.

2.3. Complete flotation model

After providing the analytical expressions of all relevant force components, Eq. (2) can be further specified as follows:

$$m\ddot{u} = (\rho_{ls} - \rho_{eq}) \frac{\pi D^2}{4} g - \frac{6.4 \eta \dot{u}}{\log\left(\frac{d}{D}\right)} - C_{D,p} \tau_y D \quad (11)$$

where d (distance between rigid boundaries in White’s formula (9)) is reinterpreted as (average) trench width. It is henceforth assumed that only the loose material in the trench is prone to liquefaction, while the surrounding soil provides a relatively rigid constraint to the interaction between fluidised soil and floating pipe.

All the simplified model results presented below have been obtained by numerically integrating Eq. (11) using an explicit version of Newmark’s method (equivalent to the central difference scheme) (Newmark, 1959) and homogeneous initial conditions – see also the code appendix at the end of this paper.

Fig. 3 shows an example of the pipe displacement and velocity as predicted by the proposed simplified model. The figure shows the attainment of the so-called ‘terminal velocity’, i.e., of steady pipe motion with $-W + F_B - F_D = 0$.

For the proposed simplified model to be fully applicable, a direct relationship between the plastic drag coefficient, $C_{D,p}$, and the Bingham number, B_n , must be introduced in Eq. (8). Indeed, the existence of such a relationship is suggested by a number of previous studies for the total drag coefficient $C_D = F_D/\tau_y D$ (De Besses et al., 2003; Tokpavi et al., 2008; Jossic and Magnin, 2009; Nirmalkar et al., 2012). Heuristically, note that, for relatively low B_n values, the viscous drag (Eq. (9)) is negligible compared to the plastic component (Eq. (8)), so that $C_D \approx C_{D,p}$.

The detailed calibration of Eq. (8) has been performed by seeking close agreement between the terminal pipe velocities predicted by the simplified model and complete 2D PFEM simulations. To this end,

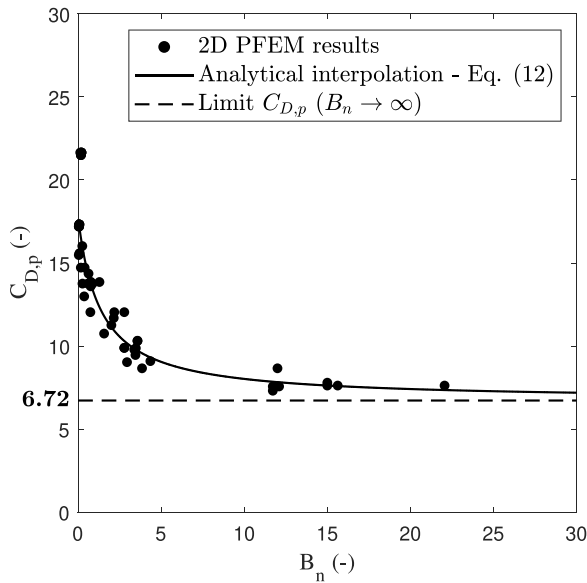


Fig. 4. Plastic drag coefficient versus Bingham number: analytical interpolation of 2D PFEM results (Eq. (12)).

extensive parametric studies have been executed for varying geometry settings ($3 < d/D < 25$ and $3.5 < b/D < 19.5$), yield stress ($10 \text{ Pa} < \tau_y < 300 \text{ Pa}$) and dynamic viscosity ($1000 \text{ Pa s} < \eta < 4000 \text{ Pa s}$). In conclusion, the comparison between simplified model and PFEM results has enabled the calibration of the following $C_{D,p}(B_n)$ function:

$$C_{D,p} = \frac{6.72B_n + 23.76}{B_n + 1.34} \quad (12)$$

Fig. 4 shows how Eq. (12) achieves satisfactory interpolation of the $C_{D,p}$ values obtained from PFEM terminal pipe velocities (black circular markers).

As mentioned in Section 2.2, the formulation of the plastic drag equation (Eq. (8)) has been partly inspired by the analogy with the (static) soil resistance to pipe uplift. Therefore, it seems logical to expect the plastic drag force from Eq. (8) to be compatible with the force returned by Eq. (7) as quasi-static conditions are approached – i.e., as $B_n \rightarrow \infty$. Remarkably, the uplift resistance factor in Eq. (12) equals 6.72 as $B_n \rightarrow \infty$, which is strongly consistent with the recommendation of DNV (2021b) for rough pipes (i.e., with no pipe–fluid slip along the pipe perimeter) in the presence of time-dependent soil behaviour and progressive failure — all these effects are inherently accounted for by the adopted 2D PFEM model. It is also worth recalling that the mentioned parametric studies have not considered cases with very shallow pipe embedment, which has led to find the depth-independent $C_{D,p}(B_n)$ function in Eq. (12). Such a formulation has been deemed appropriate to interpret the whole set of PFEM simulation results, also in light of the much larger uncertainties associated with the identification of liquefied soil’s rheological parameters — see Section 2.5.

2.4. Inclusion of pore pressure evolution effects

The formulation of Eq. (11) relies on the assumption of fully liquefied soil, which is in turn associated with the concept of nil intergranular forces (due to pore pressure build-up) and facilitates the adoption of a one-phase CFD framework (Pisanò et al., 2020). However, the liquefied state of a sand does not last indefinitely, as the gradual dissipation of the excess pore pressures leads to restoring non-vanishing mean effective stresses (p') and, therefore, (part of) the original shear strength/stiffness. As a result, the soil tends to transit back from fluid-like to solid-like state/behaviour. While detailed two-phase modelling

of a such a transition would detract from the intended simplicity of the analysis (Vescovi et al., 2020; Marveggio et al., 2021), the recent approach by Pisanò et al. (2020) preserves the simplified one-phase framework by introducing phenomenological evolution laws for η and τ_y , so as to mimic their increase with p' during reconsolidation. Based on available experimental evidence (Nishimura et al., 2002; Gallage et al., 2005; Guoxing et al., 2016), the following relationships have been proposed for the post-liquefaction viscosity and yield stress:

$$\eta = \eta_0(r_u = 1) + \eta_{rec}(r_u, p') \quad (13)$$

$$\tau_y = \tau_{y,0}(r_u = 1) + \tau_{y,rec}(r_u, p') \quad (14)$$

where $\tau_{y,0}$ and η_0 are material parameters related to fully liquefied conditions (i.e., to $r_u = 1$, where r_u is the ratio between the current pore pressure and the pre-liquefaction effective mean stress, p'_0); $\tau_{y,rec}$ and η_{rec} quantify the variation in rheological properties during reconsolidation. $\tau_{y,rec}$ may be physically associated with the recovering shear strength:

$$\tau_{y,rec} = A_{\tau_y} p' \approx \frac{M}{\sqrt{3}} p' \quad (15)$$

where the strength recovery parameter, A_{τ_y} , is linked to the critical stress ratio, M , of the soil. In fact, the physical equivalence between yield stress and undrained strength is fundamentally motivated by the frictional nature of soil behaviour, which implies the dependence of the shear strength – when expressed as an absolute shear stress value – on the current effective confinement, as well as on the previous stress path. This fact is simply reproduced by Eq. (15) in agreement with critical state soil mechanics principles (Wood, 1990), in a fashion that enables consistent representation of the quasi-static shear resistance as the soil state evolves towards liquefaction (while pore pressures build up) or reconsolidation (while pore pressures dissipate).

As for the increase in viscosity during reconsolidation, the term η_{rec} in Eq. (13) has been linearly related to p' through the material parameter A_η , based on the approach of Pisanò et al. (2020) inspired by existing experimental evidence (Gallage et al., 2005):

$$\eta_{rec} = A_\eta p' \quad (16)$$

Following the same rationale, the opposite transition may be also reproduced, except for the fact that p' undergoes an opposite evolution (from larger to lower values) when total liquefaction is gradually approached from a (more) consolidated state. It is evident that the implementation of the above approach requires as an input the evolution in space and time of the mean effective pressure, p' , which in turn depends on the excess pore pressure. Pore pressure variations may either come from a parallel numerical analysis (as discussed in Pisanò et al., 2020 and later recalled in Sections 4.1 and 4.3) or from measured experimental data (see Section 4.2), with no *a priori* limitations on the space distribution of the evolving pore pressure field. In the former case, a non-linear soil consolidation model should be adopted to account for the drastic variations in stiffness and permeability at low mean effective stresses — see, for instance, the non-linear model adopted by Pisanò et al. (2020).

The general setup of the proposed calculation scheme is summarised in Algorithm 1, based on a simple explicit time integration scheme. It is remarked that the evolution in space and time of the pore pressures is an external/decoupled input to the pipe-soil interaction analysis as formulated in Eq. (11).

2.5. Calibration of liquefied sand parameters

Central to the application of the proposed modelling framework is the calibration of liquefied sand’s parameters, i.e., viscosity and yield stress. Following decades of extensive studies, broad consensus seems to have been achieved about the extreme variability of such parameters, particularly of the viscosity — this aspect is clearly pointed out, to name a few, by Tamate and Towhata (1999), Parsons et al. (2001), Hwang et al. (2006) and Montassar and de Buhan (2013). Multiple factors contribute to such variability:

Algorithm 1 Numerical solution scheme for pipe flotation analysis

```

Initialise geometry settings and soil properties
Compute pipe weight,  $W$ , through Eq. (3)
Compute buoyancy force,  $F_B$ , through Eq. (4)
while  $t \leq T_{final}$  do                                > Loop over time
  if Pipe entirely below soil surface then
    Obtain pore pressure and mean effective stress at pipe centroid
    Update soil viscosity and yield stress through Eqs. (13)–(14)
    Compute plastic drag force,  $F_{D,p}$ , through (8)
    Compute viscous drag force,  $F_{D,v}$ , through Eq. (9)
    Compute total drag force,  $F_D = F_{D,v} + F_{D,p}$ 
    Compute pipe acceleration,  $\ddot{u}$ , by solving Eq. (11)
    Compute pipe velocity/displacement,  $\dot{u}$  and  $u$ 
    Update location of pipe centroid
  end if
end while
    
```

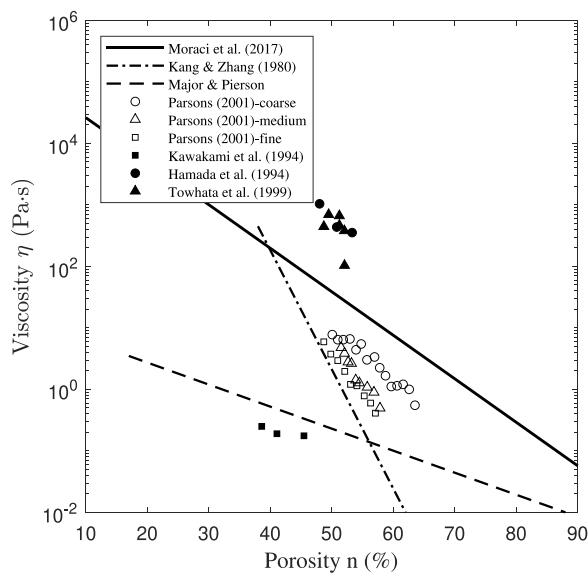


Fig. 5. Scatter of viscosity values from previous studies.

- *Variety of laboratory testing procedures.* Rheological properties may be identified via very diverse testing procedures, including the use of viscometers (Kawakami et al., 1994) or flumes (Parsons et al., 2001), dam-breaking tests (Della Vecchia et al., 2019), back-analysis of the interaction with objects such as spherical balls (Hamada et al., 1993; Kawakami et al., 1994; Hwang et al., 2006), cylindrical bars (Hwang et al., 2006) and pipes (Hamada et al., 1993; Towhata et al., 1999). Different testing procedures entail diverse flow regimes and rheological responses;
- *Influence of mixture composition.* Rheological properties are known to be extremely sensitive to the composition, grain size distribution, and porosity (or relative density) of the soil–water mixture (Parsons et al., 2001; Pierson, 2005);
- *Rheological assumptions.* The rheology of liquefied sand does not necessarily adhere to simplified modelling assumptions (Ancy, 2007). Deviations of real behaviour from such assumptions will impact the resulting rheological characterisation, or require more complex modelling (e.g., from Bingham to Herschel–Bulkley rheology).

Fig. 5 provides further insight into the scatter in the literature of viscosity values for fully liquefied soil (i.e., with $r_u = 1$), also in comparison to the empirical relationships proposed by Kang and Zhang (1980), Major and Pierson (1992), Moraci et al. (2017). Literature data

for sandy mixtures have been selected to span typical values of initial porosity in the 35%–65% range, and to represent the influence of different (i) grain size distribution and fine content, (ii) testing procedure (flume tests, viscometer, lateral spreading, interaction with rigid pipe) and (iii) conceptual interpretation (Bingham modelling against Newtonian modelling with ‘equivalent viscosity’). Fig. 5 confirms variations in viscosity over 5 orders of magnitude. Values of equivalent viscosity obtained through the assumption of Newtonian behaviour – such as those reported by Towhata et al. (1999) – lie, as expected, on the high side of the spectrum.

Similar considerations apply to the determination of the fully liquefied shear strength (i.e., the yield stress in this context), which is still an open issue for fully liquefied soils. According to the notion of steady-state deformation (see, e.g., Poulos, 1981), the shear strength of a liquefied soil is mainly a function of the relative density (or porosity), being the influence of other initial conditions largely erased by the deformation process; other studies, nonetheless, have also emphasised the influence of the stress path to liquefaction (Vaid and Thomas, 1995). For many soils in fully liquefied conditions, the dependence of their shear strength on the relative density is so large that even very small variations in density may lead to completely different strength values.

If sandy soils could be sampled ‘undisturbed’ from the site, then the liquefied shear strength could be measured through undrained triaxial tests on soil specimens consolidated up to the relevant effective stress state. Unfortunately, well-known difficulties in obtaining undisturbed sand samples and the mentioned sensitivity of the liquefied strength to density would make this effort unfruitful. Conversely, different approaches have been proposed to estimate the liquefied shear strength, including (i) use of the laboratory steady-state strength corrected to account for site conditions (Poulos et al., 1985), (ii) direct correlation to in-situ data based on relevant case histories (Stark and Mesri, 1992; Olson and Stark, 2002), or (iii) resort to the notion of residual stress ratio (Ishihara, 1993). Despite the acknowledged uncertainties, the yield stress of a fully liquefied sand is generally believed to range from tens to a few hundreds Pa (Uzuoka et al., 1998; Parsons et al., 2001; Pierson, 2005; Gallage et al., 2005) – therefore, not extremely influential in soil–structure interaction problems involving strong reconsolidation effects.

Accurate determination of the above reconsolidation parameters (Eqs. (14)–(15)) within the proposed total stress framework will require further development in laboratory testing at very small confinement (Gallage et al., 2005) – along this direction, the work of Towhata et al. (2009) on testing in a zero-gravity environment is particularly worthy of mention.

3. Comparison to 2D PFEM results

Following the calibration of Eq. (8), the simplified model (henceforth, SM) has been verified against a set of 2D PFEM results. To this end, a fully liquefied backfill material has been considered, i.e., with no evolution of the rheological parameters. Fig. 6 shows the geometry of the reference domain and a magnified view of the computational triangular mesh around the pipe. Other relevant computational settings include: (i) average element size equal to 0.02 m, resulting in approximately 52000 nodes; (ii) time step size and total physical simulation time equal to 0.04 s and 8 s, respectively; (iii) fixed bottom and lateral boundaries, no pipe–fluid slip along the pipe perimeter, and free top boundary. The general soundness of the obtained PFEM results is exemplified for a selected simulation case in Fig. 7 – see parameter settings in Table 1, with the sole exception of $\tau_y = 100$ Pa. The figure illustrates on the left the final colour map of the r_τ ratio between the Euclidean norm of the deviatoric stress tensor ($\|\tau\| = \sqrt{\tau : \tau}$) and the yield stress τ_y – values of this ratio that are lower or larger than 1 define deviatoric stress states, respectively, below and above the yielding limit. The dark area around the pipe is associated with $r_\tau > 1$, which

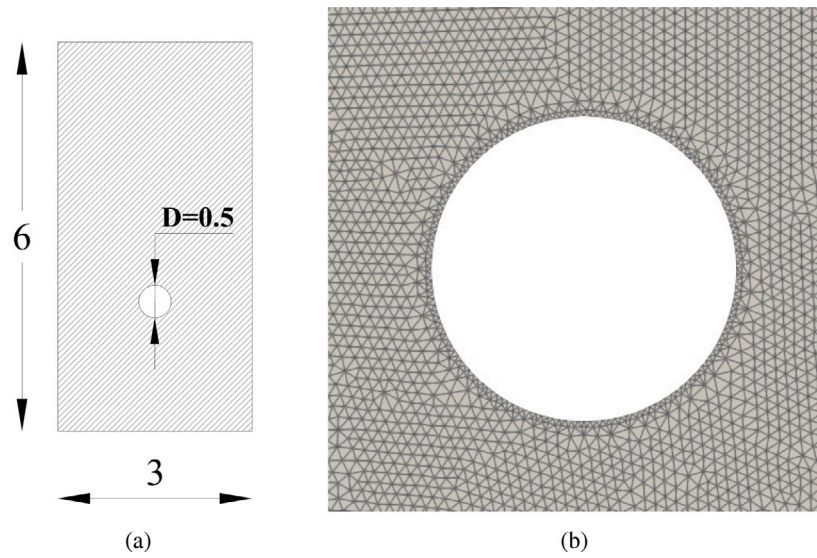


Fig. 6. PFEM model of the reference verification case: (a) geometry (dimensions in meters) and (b) magnified mesh around the pipe cross-section.

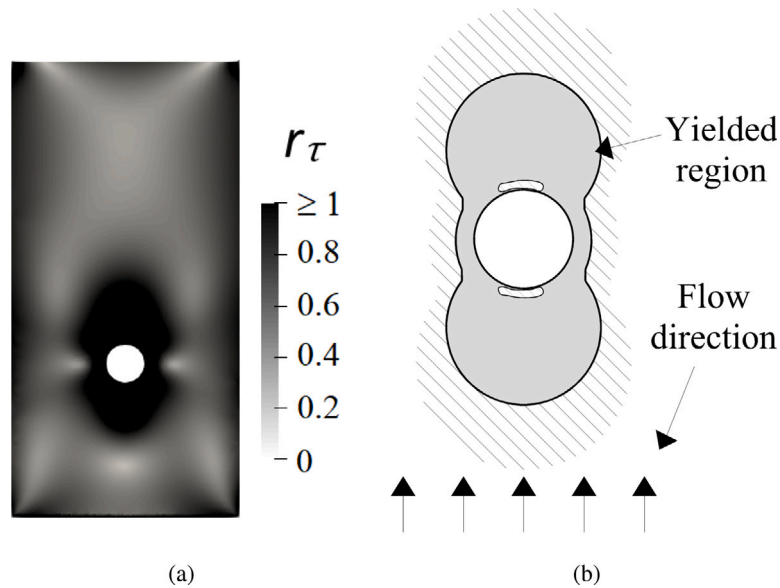


Fig. 7. Fluid yielding around the pipe: (a) final ratio between Euclidean deviatoric stress tensor norm and yield stress associated with $B_n \approx 3.5$ during pipe flotation; (b) distribution of fluid yielding around a pipe subjected to uniform flow for $B_n = 10$ – redrawn after Adachi and Yoshioka (1973).

Table 1
Geometrical and mechanical parameters for the reference verification case in Fig. 6.

D (m)	d/D (-)	b/D (-)	ρ_{eq} (kg/m ³)	ρ_{ls} (kg/m ³)	η (Pa·s)	τ_y (Pa)
0.5	6	3.75	1482	1800	2000	50

are spatially distributed in a manner similar to the previous findings of Adachi and Yoshioka (1973), De Besses et al. (2003), and Mitsoulis (2004).

Six sets of PFEM and SM parametric analyses have been performed, each featuring realistic variations of the parameter set in Table 1 and in all cases with $2 < b/D < 9.5$:

- Set 1 → liquefied sand density varied over the range $\rho_{ls} = [1700; 2000]$ kg/m³

- Set 2 → dynamic viscosity varied over the range $\eta = [1500; 5000]$ Pa·s
- Set 3 → yield stress varied over the range $\tau_y = [10; 150]$ Pa
- Set 4 → pipe diameter varied over the range $D = [0.1; 1.5]$ m
- Set 5 → trench width ratio over the range $d/D = [3; 12]$
- Set 6 → $\rho_{pipe} = 950$ kg/m³ (HDPE) and $\rho_{pipe} = 7800$ kg/m³ (steel).

Fig. 8 shows excellent agreement between the terminal velocities returned by SM and PFEM simulations for all the mentioned cases — particularly, for a resulting range of the Bingham number between 10^{-2} and 10^1 . To further corroborate the suitability of the proposed model formulation, the SM relationship between the normalised total drag force (i.e., viscous + plastic) and the Bingham number is compared in Fig. 9 to the previous results by Mitsoulis (2004) (in grey, as previously reported in Fig. 2). The excellent qualitative agreement between SM

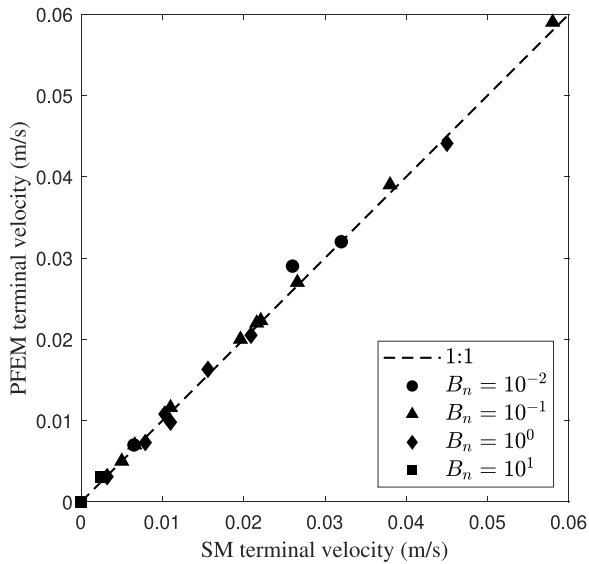


Fig. 8. Comparison between SM and PFEM terminal velocities — distinct markers are adopted for different values of the Bingham number.

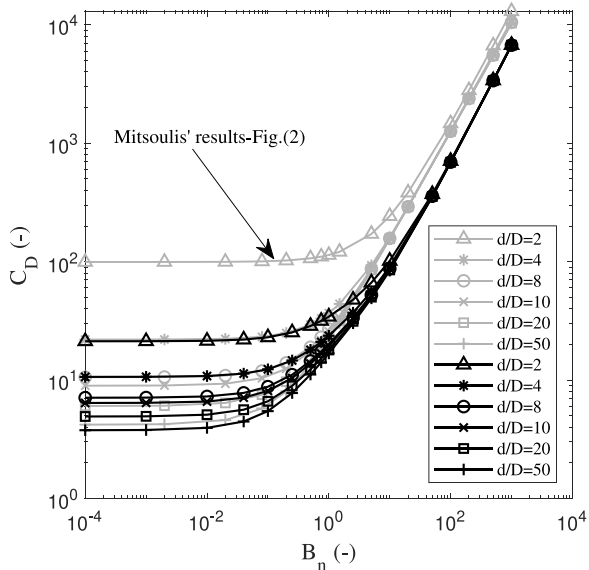


Fig. 9. SM trends of normalised drag force versus Bingham number for different ratios between rigid boundary distance and diameter of the floating pipe. The corresponding curves in Fig. 2 by Mitsoulis are reported in grey.

and Mitsoulis' trends confirms the ability of the proposed model to reproduce the physics of the problem. Quantitative differences, most pronounced for low B_n values (fast motion regime) and d/D ratio, are likely due to the different setups of the two reference problems, i.e., upward pipe flotation in a constrained trench against uniform horizontal flow around a cylinder between two rigid boundaries.

4. Validation against small-scale test data

The proposed simplified model has been finally validated against the results of selected small-scale experiments from the literature. In particular, three sets of test data have been considered, namely regarding the cases of: (i) pipe flotation in liquefied reconsolidating sand (Horsten, 2016); (ii) pipe flotation induced by incipient sand liquefaction triggering (Miyamoto et al., 2020); (iii) lateral pipe dragging

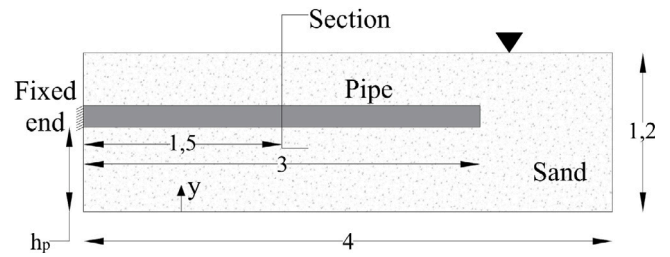


Fig. 10. The experimental pipe flotation setup adopted by Horsten (2016) (dimensions in meters).

Table 2

Pipe geometrical and mechanical properties: h_p =elevation; L_p =length; t_p =cross-section thickness; D_p =outer diameter; I_p =cross-section moment of inertia; ρ_p =HDPE mass density; E_p =HDPE Young's modulus.

	h_p (mm)	L_p (m)	t_p (mm)	D_p (mm)	I_p (m ⁴)
Pipe 1	790	3	17	110	$5.6 \cdot 10^{-6}$
Pipe 2	640	3	33	160	$2.8 \cdot 10^{-5}$
	$\rho_p=950 \text{ kg/m}^3 \quad E_p=1100 \text{ MPa}$				

in reconsolidating sand (Towhata et al., 1999). While cases (i) and (iii) have been previously simulated within the complete 2D PFEM framework (Pisanò et al., 2020), original SM results are presented in what follows to demonstrate the ability of the new model to achieve similar accuracy with negligible computational costs.

4.1. Pipe flotation in liquefied reconsolidating sand

The original pipe flotation experiments reported by Horsten (2016) were executed in a large container (length = 4 m, width = 2.5 m, depth = 1.2 m). Fast liquefaction of loose sand was achieved, after a fluidisation-reconsolidation cycle, through the impact of a falling weight on the sidewall of the sand container — the occurrence of liquefaction was confirmed both by visual inspection and pore water pressure measurements at pre-selected soil locations. All tests were performed in Ittebeck sand, which is a uniform fine sand characterised by specific grain density $G_s = 2.64$, $d_{50} = 0.165$ mm (median grain diameter), $e_{max} = 0.868$ and $e_{min} = 0.527$ (maximum/minimum void ratio). Three different high-density polyethylene (HDPE) flexible pipes, with different outer diameter and thickness, were used. The experimental setup illustrated in Fig. 10 featured a fixed-end pipe buried in a saturated sand layer — an edge of the pipe was clamped to more realistically represent a pipeline connected to an existing structure. Geometrical and mechanical properties of the HDPE pipes are listed in Table 2. The domain width used in Pisanò et al.'s PFEM simulations was equal to 1.5 m, which is the same value preserved for d (boundary distance) in Eq. (9).

The evolution of sand's rheological parameters upon reconsolidation has been fed to the simplified model based on the approach discussed in Section 2.4. The space-time evolution of the excess pore pressures within the sand layer has been estimated through a one-dimensional non-linear consolidation model, in a fashion identical to that described by Pisanò et al. (2020). The parameters governing the consolidation model have been calibrated against independent pore pressure dissipation data provided by Horsten (2016), and are reported for convenience in Table 3. Since the proposed model is geometrically zero-dimensional, a single location in the parallel 1D consolidation model had to be selected for extracting the time evolution of p' . To this end, p' values associate with the (moving) location of the pipe centroid have been used to update the values of η and τ_v (via Eqs. (13)–(14)) and enable the evaluation of the drag force in reconsolidating soil. As is shown in Table 4, it has been possible to obtain a calibration of the SM model

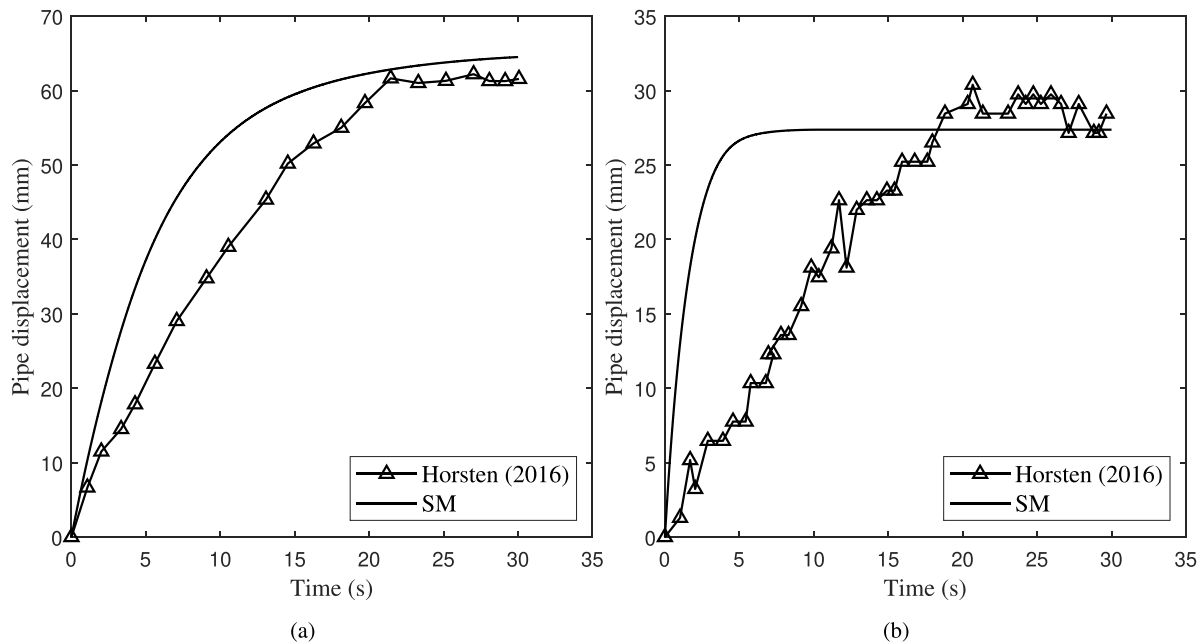


Fig. 11. Pipe’s flotation: comparison between experimental data from Horsten (2016) and simplified model prediction for (a) pipe 1 and (b) pipe 2 – see Table 2. Displacement measured/simulated at the midsection of each pipe.

Table 3
Consolidation model parameters calibrated against data from Horsten (2016).

H (m)	γ (kN/m ³)	C_T (m/s)	e_0 (-)	χ (-)	α (-)	σ'_{ref} (kPa)
1.2	18.4	$4 \cdot 10^{-4}$	0.88	1038	1.15	100

Table 4
(Enhanced) Bingham parameters used to reproduce measurements from pipe flotation tests in liquefied reconsolidating sand.

A_η (Pa·s/Pa)	A_{τ_y} (-)	η_0 (Pa·s)	$\tau_{y,0}$ (Pa)
20	$0.69 \left(= \frac{1.2}{\sqrt{3}} \right)$	2200	0

that adopts the same set of rheological/reconsolidation parameters previously identified by Pisanò et al. (2020).

Along with the reconsolidation mechanism, a specific modification of the simplified model has also been introduced to refine the representation of the test setup in Fig. 10, particularly of the clamped edge of the cantilever pipe. As described in Pisanò et al. (2020), a simplified procedure was devised to preserve the computational benefits of reduced-order modelling (in lieu of fully 3D), while accounting for elastic and boundary effects through an elastic restoring force introduced on the right side of Eq. (2). The elastic force associated with the midsection of the cantilever pipe (see relevant cross-section in Fig. 10) was identified based on standard structural analysis:

$$F_E = \frac{384}{17} \frac{E_p I_p}{L^4} (y_c - y_{c,0}) \quad (17)$$

where $y_{c,0}$ and y_c are the initial and current elevation of the pipe centroid, while L is the distance between the clamped edge and the considered mid-section – the values of the pipe’s Young’s modulus (E_p) and cross-sectional inertia (I_p) are provided in Table 2. It is worth noting that, while structural 3D effects were accounted for through the F_E term, the same modelling of the fluid drag force based on 2D/plane-strain studies was retained – i.e., by disregarding a possible influence of the clamped connection on the stress and velocity fields in the fluid. Obviously, the determination of the structural restoring force F_E should be included in Algorithm 1 whenever appropriate.

Fig. 11 shows very good agreement between experimental data and SM results for two different pipe flotation experiments, especially in terms of final pipe displacement. As for the transient displacement branch, significant influence of the clamped boundary condition is to be noted, which hindered full-depth validation of the rheological terms.

To foster the industry uptake of the proposed flotation analysis approach, the original Matlab code developed for the simulation of Horsten’s tests is shared in the final appendix.

4.2. Pipe flotation during wave-induced sand liquefaction

A second validation case, the experimental data provided by Miyamoto et al. (2020) have been considered. The original pipe flotation experiments were executed in a drum centrifuge equipped with a system capable of generating wave-induced sand liquefaction – a centrifugal acceleration equal to 70 g was adopted throughout the experimental study. All tests were executed in silica sand No. 7, which features $G_s = 2.66$, $d_{50} = 0.15$ mm, $e_{max} = 1.16$, $e_{min} = 0.7$, and unit weight $\gamma = 18.3$ kN/m³ – with reported values of relative density equal to 35–38%. The model pipeline comprised an aluminium pipe ($D = 25$ mm) filled with urethane foam, which overall resulted in a specific gravity of the model pipe G_p equal to 1.35. The authors used the acceleration factor, $N = 70$, to relate dimensions and measurements to the scale of the assumed prototype – see Fig. 12).

The liquefaction of the sand sample in the centrifuge was obtained by applying cyclic wave loading – particularly, metolose was used as pore fluid in order to match the time-scaling laws of soil consolidation and fluid wave propagation. The corresponding pore pressure build-up, which gradually induced sand liquefaction and then pipe flotation, was measured during the tests and used herein to directly inform the proposed flotation model – the so-called Case-3 in Miyamoto et al. (2020) has been considered herein. Fig. 13 exemplifies the good agreement between selected interpolation functions (curve-fitting) and the (upscaled) excess pore pressures (u_e) along the soil depth coordinate (z , normalised with respect to the soil layer thickness, H).

After setting the space/time evolution of u_e (and accordingly of p') as an input to the pipe flotation analysis, distinct PFEM and SM simulations have been performed for more thorough validation of the whole framework, in combination with the following parameters:

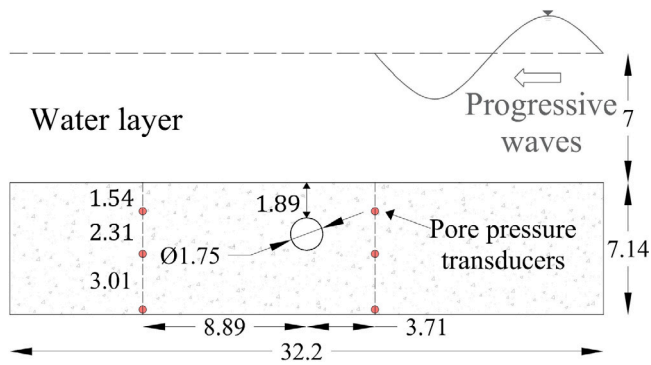


Fig. 12. The experimental setup adopted by Miyamoto et al. (2020) to simulate wave-induced sand liquefaction and pipe flotation (dimensions in meters).

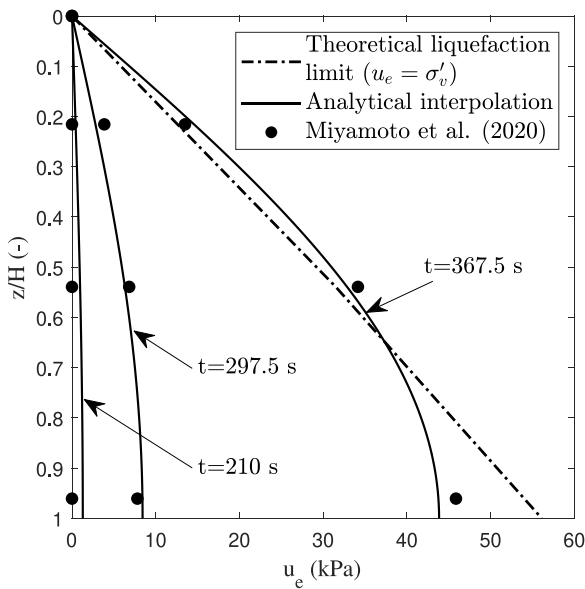


Fig. 13. Isochrones of excess pore pressure (u_e) at different time different times: measured (upscaled) data vs analytical interpolation — data from Miyamoto et al. (2020), Case-3. Vertical effective stress distribution obtained based on $\gamma' = 8.3 \text{ kN/m}^3$ (soil buoyant unit weight).

- γ (liquefied soil unit weight) directly obtained from measured data;
- $\eta_0 = 2000 \text{ Pa}\cdot\text{s}$ selected for $D_r = 35\%$ based on Hwang et al. (2006);
- $A_{r_y} = 0.77$ set according to Eq. (15) using $M = 1.33$, which corresponds with a critical friction of approximately 33° (Schmertmann, 1978);
- $A_\eta = 20 \text{ Pa}\cdot\text{s}/\text{Pa}$ assumed based on observations provided by Pisanò et al. (2020) for a similar sand;
- $\tau_{y,0} = 940 \text{ Pa}$ identified to reproduce the experimental flotation velocity of the pipe, approximately equal to 24 mm/s .

It is worth mentioning that $\tau_{y,0}$ and η_0 had to be jointly calibrated by trial-and-error. Compared to the simplification of nil $\tau_{y,0}$ adopted in Section 4.1, a more reasonable value of η_0 has been obtained by using a non-nil yield stress value for the sand in its fully liquefied state. In this respect, the rather low embedment of the model pipe tested by Miyamoto et al. ($b/D = 1.08$, see Fig. 12) may have played a role, possibly due to neglecting in Eq. (12) the depth-dependence of the plastic drag coefficient as the floating pipe approaches the soil surface.

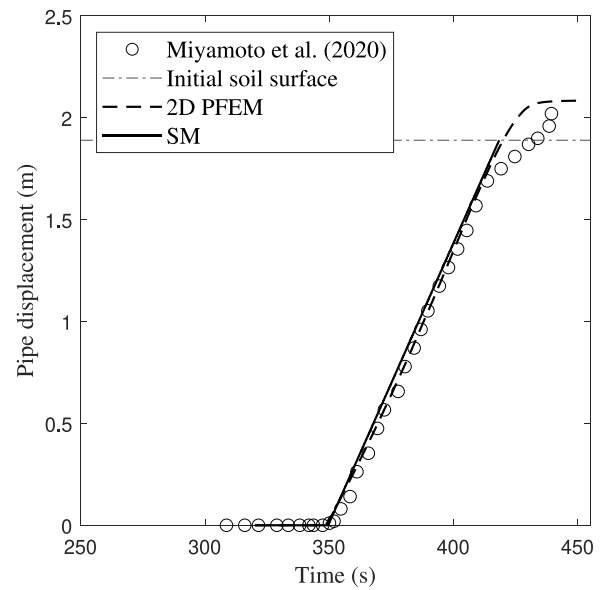


Fig. 14. Wave induced-pipe flotation: SM vs PFEM predictions of the upward pipe displacement — data from Miyamoto et al. (2020), Case-3.

Using identical soil parameters, very consistent SM and PFEM results have been obtained for the experimental test at hand – all results/data presented in prototype scale. Fig. 14 shows satisfactory agreement between the two model responses in terms of pipe displacement versus time, which also capture very closely the experimental measurements. In the real experiment, the flotation is eventually arrested by the larger density of the pipe with respect to that of the fluid overlaying the sand deposit. While this occurrence is correctly reproduced by the more advanced PFEM model, the proposed simplified model is clearly not equipped to capture such a kind of boundary effect. This is an intrinsic limitation of the proposed approach, which however remains very convenient for inexpensively predicting the timing of pipe flotation.

4.3. Pipe dragging in liquefied reconsolidating sand

Finally, the simplified model has been further validated against the results of lateral pipe dragging experiments reported by Towhata et al. (1999). Reference is made to a 1 g test in which a pipe buried in extremely loose saturated sand was laterally dragged after full soil liquefaction (induced by a strong shaking of the container). The experiment was carried out in Toyoura sand of $G_s = 2.65$, $d_{50} = 0.17 \text{ mm}$, and initial void ratio equal to $e_0 = 1.04$ ($D_r = 30\%$). A model pipe featuring 30 mm diameter and 300 mm length was embedded at a depth of 300 mm depth into a sand sample of 500 mm thickness. After the attainment of soil liquefaction, the pipe was laterally dragged with a velocity of 8 mm/s during the concurrent reconsolidation of the sand.

From a modelling standpoint, the pore pressure dissipation process in the sand layer has been reproduced using the same non-linear consolidation model mentioned in Section 4.1, after calibration against Towhata et al.'s experimental data as per Pisanò et al. (2020). Table 5 reports the set of calibrated consolidation parameters, while the parameters associated with the enhanced Bingham model are listed in Table 6 after slight re-calibration (particularly for A_η). As reported (Pisanò et al., 2020), A_{r_y} is broadly related – via Eq. (15) – to the critical friction angle of the sand, whereas A_η has been identified within the relatively narrow range inferred from the experimental data of Gallage et al. (2005). While sand's steady-state undrained shear strength may be rather small – though not nil – after full liquefaction (see Section 2.5), it has been convenient to set $\tau_{y,0} = 0$ in light of (i) the

Table 5
Consolidation model parameters calibrated against data from Towhata et al. (1999).

H (m)	γ (kN/m ³)	C_T (m/s)	e_0 (-)	χ (-)	α (-)	σ'_{ref} (kPa)
0.5	17.7	$4 \cdot 10^{-4}$	1.04	18	0.5	100

Table 6
(Enhanced) Bingham parameters used to reproduce measurements from a lateral pipe dragging tests in liquefied reconsolidating sand.

A_η (Pa·s/Pa)	A_{τ_y} (-)	η_0 (Pa·s)	$\tau_{y,0}$ (Pa)
6	0.69	300	0

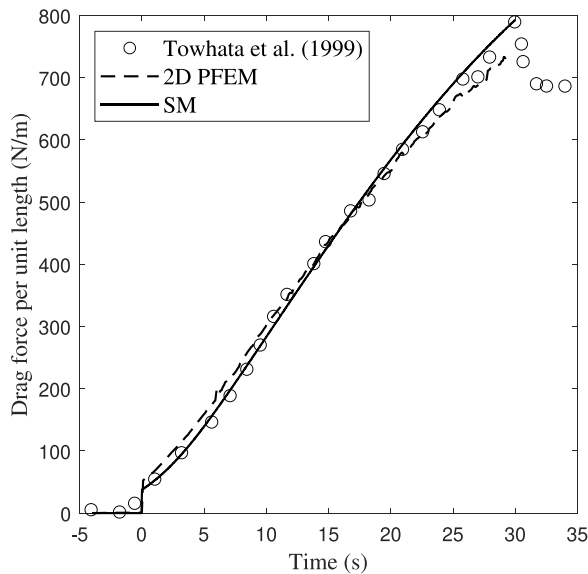


Fig. 15. Lateral pipe dragging: comparison between drag force per unit length measured in the experiments and predicted with the simplified model — data from Towhata et al. (1999).

extremely low density of the sand sample, and (ii) the vanishing initial effective stresses associated with the very shallow embedment of the pipe in the reference 1 g model – only 300 mm (Towhata et al., 1999).

Fig. 15 shows the excellent ability of Takaisi’s formula (Eq. (10)) to reproduce the measured drag force, on condition that the enhancement of sand’s rheological properties due to reconsolidation is taken into account — as discussed in detail by Pisanò et al. (2020). Also in this validation case, the results in Fig. 15 indicate very satisfactory agreement between SM and PFEM predictions.

5. Concluding remarks

This paper has presented a simplified model for the analysis of the interaction between floating pipelines and liquefied sand, also accounting for transient liquefaction and/or reconsolidation effects in the soil. Following the same one-phase, total stress approach presented in Pisanò et al. (2020), the soil has been modelled as a Bingham fluid, with rheological parameters possibly updated in space and time based on a decoupled pore pressure evolution analysis. The forces governing pipe flotation have been formulated using spreadsheet-friendly analytical relationships, with relevant insight provided into their calibration and use. The final outcome is a practice-oriented model that can be utilised

to predict the upward motion of (a selected cross-section of) a floating pipe in liquefied sand.

The soundness and accuracy of the new model has been explored by comparing to the results of more complete 2D PFEM simulations and small-scale experimental data from the literature. Among other aspects, it has been shown that capturing the variation in viscosity and yield stress induced by excess pore pressure changes enables accurate evaluation of pipe–fluid interaction forces, and in turn of the pipe displacement from flotation trigger to arrest.

Future users should bear in mind the role played by the relative duration (and distance in time) of soil reconsolidation with respect to the main liquefaction-inducing event. Two main cases of practical relevance are envisaged: (i) if the liquefaction-inducing event clearly precedes the onset of pipe flotation, then reconsolidation effects should be accounted for in the analysis; (ii) if pipe flotation is mostly concurrent with the occurrence of soil liquefaction, then considering fully liquefied soil behaviour appears to be more appropriate, i.e., with no update of soil’s rheological properties.

Both novelty and applicability of this work relate to the development of a flotation modelling framework that can be applied with considerably fast computations. Among the limitations of the proposed approach, geometrical reduction is probably the most prominent, in that it does not allow the consideration of 2D/3D effects related to, for instance, spatial variability and more complex boundary/loading conditions. Nevertheless, this work is believed to make a valuable contribution to the practical engineering of marine pipelines, particularly with regard to the analysis and prevention of liquefaction-related risks.

Codes

Matlab code developed for the analysis of the validation case in Section 4.1

CRediT authorship contribution statement

F. Pisanò: Conceptualization, Methodology, Supervision, Writing – original draft. **D. Betto:** Conceptualization, Methodology, Software, Validation, Formal analysis, Data curation, Writing – original draft. **G. Della Vecchia:** Conceptualization, Methodology, Supervision, Writing – original draft. **M. Cremonesi:** Funding acquisition, Methodology, Supervision, Software, Writing – review & editing.

Declaration of competing interest

The authors declare the following financial interests/personal relationships which may be considered as potential competing interests: Davide Betto and Massimiliano Cremonesi reports financial support was provided by Government of Italy Ministry of Education University and Research.

Data availability

Data will be made available on request.

Acknowledgements

Davide Betto and Massimiliano Cremonesi gratefully acknowledge the support of the Italian Ministry of University and Research through the project PRIN2017 XFASTSIMS: Extra fast and accurate simulation of complex structural systems (D41F19000080001).

```

1  %%%%%%%%%%%%%%%%%%%%%%%%%%%%%%%%%%%%%%%%%%%%%%%%%%%%%%%%%%%%%%%%%%%%%%%%%
2  %%%%%%%%%%%%%%%%%%%%%%%%%%%%%%%%%%%%%%%%%%%%%%%%%%%%%%%%%%%%%%%%%%%%%%%%%
3  %%%%%%%%%%
4  %%%%%%%%%% Validation against Horsten (2016)'s experimental data (Sec. 4.1) %%%%%%%%%%
5  %%%%%%%%%% Authors: Pisano F., Betto D., Della Vecchia G. and Cremonesi M. %%%%%%%%%%
6  %%%%%%%%%%
7  %%%%%%%%%% Year: 2022 %%%%%%%%%%
8  %%%%%%%%%%%%%%%%%%%%%%%%%%%%%%%%%%%%%%%%%%%%%%%%%%%%%%%%%%%%%%%%%%%%%%%%%
9  %%%%%%%%%%%%%%%%%%%%%%%%%%%%%%%%%%%%%%%%%%%%%%%%%%%%%%%%%%%%%%%%%%%%%%%%%
10
11 %%%%%%%%%%%%%%%%%%%%%%%%%%%%%%%%%%%%%%%%%%%%%%%%%%%%%%%%%%%%%%%%%%%%%%%%% INPUT SECTION %%%%%%%%%%%%%%%%%%%%%%%%%%%%%%%%%%%%%%%%%%%%%%%%%%%%%%%%%%%%%%%%%%%%%%%%%
12
13 g=9.81; %m/s^2
14
15 %%%% PIPE DATA (assumed empty)
16 t=17/1000; %m thickness of the pipe
17 D_e=0.11; %m outer diameter
18 D_t=D_e/t;
19 D_in=D_e-2*(D_e/D_t); %m inner diameter
20 Atot=pi*0.25*D_e^2; %m2 cross-section area
21
22 rho_pipe=950; %kg/m^3 density of pipe material
23 gamma_pipe=rho_pipe*g; %N/m^3
24 gamma_eq=gamma_pipe*(D_e^2-D_in^2)/D_e^2; %N/m^3
25 rho_eq=gamma_eq/g; %kg/m^3
26 E=1100*10^6; %Pa Young Modulus of pipe material
27 I=pi/64*(D_e^4-D_in^4); %m^4 moment of inertia
28 L=3; %m pipe length
29
30 %%%% GEOMETRY
31 H=1.2; %m soil layer thickness
32 h=0.79; %m pipe elevation
33 cover=H-D_e-h; %m
34 d_D=1.5/D_e; %
35
36 %%%% LIQUEFIED SOIL PARAMETERS
37
38 rho_f=1.84*10*1000/g; %kg/m^3 density of the liquefied soil
39 gamma_f=rho_f*g; %N/m^3
40
41 % Fully liquefied parameters
42 eta_0=2200; %Pa*s fully liquefied viscosity
43 tau_0=0; %Pa fully liquefied yield stress
44
45 % Rheological enhancement parameters (see Eqs. (15)-(16), and also Pisano et al. (2020))
46 M=1.2;
47 Atau=M/(3^0.5);
48 Aeta=20; %Pa s/Pa
49
50 %%%% SOIL DATA FOR RECONSOLIDATION
51
52 gamma_w=9.81; %kN/m^3
53 gamma_s=gamma_f/1000; %kN/m^3
54 g_s=2.6426;
55
56 %initial void ratio calculations
57 rho_w=gamma_w*1000/9.81; %kg/m^3
58 rho_sat=gamma_s*1000/9.81; %kg/m^3
59 rho_s=g_s*rho_w; %kg/m^3
60 n_0=(rho_s-rho_sat)/(rho_s-rho_w); %initial porosity
61 e_0=n_0/(1-n_0); %initial void ratio
62
63 %1D reconsolidation parameters (see Pisano et al. (2020))
64 Ct=0.4*10^-3; %variable permeability parameter
65 s_min=0.2; %kPa effective stress threshold
66 chi=1038; %variable stiffness parameter
67 alfa=1.15; %variable stiffness parameter
68 sigma_ref=100; %kPa
69
70
71 %%%%%%%%%%%%%%%%%%%%%%%%%%%%%%%%%%%%%%%%%%%%%%%%%%%%%%%%%%%%%%%%%%%%%%%%% INITIALISATION %%%%%%%%%%%%%%%%%%%%%%%%%%%%%%%%%%%%%%%%%%%%%%%%%%%%%%%%%%%%%%%%%%%%%%%%%
72

```

```

73 %%%% INITIALISATION OF PARALLEL CONSOLIDATION ANALYSIS
74
75 dz=0.01; % grid spacing
76 m_space=round(H/dz)+1; % number of spatial gridpoints
77 z(1)=0;
78 u0(1)=0;
79 zeta(1)=H;
80
81 for k=1:m_space-1 % creating depth and u0 vectors
82     z(k+1)=dz+z(k);
83     u0(k+1)=z(k+1)*(gamma_s-gamma_w);
84     zeta(k+1)=H-z(k+1);
85 end
86
87 e0=ones(1,length(u0))*e_0; % vector of initial void ratio
88 u_initial=u0;
89
90 %%% TIME PARAMETERS
91
92 T_in=0; %s initial time
93 T_fin=30; %s final time
94 dt=0.0001; %s time step size
95
96 t=[T_in:dt:T_fin];
97
98 yc=zeros(1,length(t)); % definition of pipe centroid
99 Disp_f=zeros(1,length(t)); % pipe displacement vector
100 Vel_f=zeros(1,length(t)); % pipe velocity vector
101 Acc_f=zeros(1,length(t)); % pipe acceleration vector
102
103 %initial conditions
104 yc(1)=h+0.5*D_e;
105 Disp_f(1)=0;
106 Vel_f(1)=0;
107 Acc_f(1)=(rho_f*g*Atot-rho_eq*g*Atot-tau_0*6.72*D_e)/(rho_eq*Atot);
108
109 % Newmark's time integration parameters
110
111 beta=0;
112 gamma=1/2;
113
114 %%%%%%%%%%%%%%%%%%%%%%%%%%%%%%%%%%%%%%%%%% TIME-DOMAIN ANALYSIS (solution of Eq. (11)) %%%%%%%%%%%%%%%%%%%%%%%%%%%%%%%%%%%%%%%%%%
115
116 for i=1:(length(t)-1) % Loop over Time
117
118     if(H-((H-cover)+Disp_f(i)))>=0 % arrest computation if pipe resurfaced
119         F_p(i)=gamma_eq*Atot; %N/m Pipe weight (Eq. (3))
120         F_b(i)=gamma_f*Atot; %N/m Buoyancy force (Eq. (4))
121         F_e(i)=(384/17)*E*I/(L^4)*(yc(i)-yc(1)); %N/m Elastic force (Eq. (17))
122
123         yc(i+1)=h+D_e*0.5+Disp_f(i); %m
124         t_plot(i)=t(i); %s
125         Disp=Disp_f(i);
126
127         % Evaluation of pore pressure field at current time step
128         % ("Consolidation_Horsten" not provided - based on Pisanò et al. (2020))
129         [delta_u_loc,z_g,u1,e1,gamma_sat_loc] = Consolidation_Horsten(z,m_space,dz,
u_initial,u0,e0,H,cover,D_e,gamma_w,gamma_s,g_s,Ct,s_min,chi,alfa,sigma_ref,dt,Disp);
130         u0=u1;
131         e0=e1;
132         Delta_u(i)=delta_u_loc*1000;
133
134         % Update of rheological parameters
135         eta(i)=eta_0-Aeta*delta_u_loc*1000; % (Eq. (13))
136         tau(i)=tau_0-Atau*delta_u_loc*1000; % (Eq. (14))
137
138         % Evaluation of drag force
139         Fd_v(i)=(eta(i)*Vel_f(i)*6.4)/(log10((d_D))); %N/m Viscous drag (Eq. (7))
140
141         Bn(i)=(tau(i)*D_e)/(eta(i)*Vel_f(i)); %Bingham number
142         Cdp(i)=(6.72*Bn(i)+23.76)/(Bn(i)+1.34); %Plastic drag coeff. (Eq. (12))
143         F_dp(i)=Cdp(i)*tau(i)*D_e; %N/m Plastic drag (Eq. (10))

```

```

144     F_d(i)=Fd_v(i)+F_dp(i); %N/m Total drag (Eq. (6))
145     F_d(1)=tau_0*6.72*D_e;
146
147
148     % Newmark's series expansion
149     delta_t=(t(i+1)-t(i));
150     Acc_f(i+1)=(1/(gamma_eq*Atot/g))*(-F_p(i)+F_b(i)-F_d(i)-F_e(i));
151     Vel_f(i+1)=Vel_f(i)+(1-gamma)*delta_t*Acc_f(i)+gamma*delta_t*Acc_f(i+1);
152     if Vel_f(i+1)<0 % to avoid unphysical sinking linked to numerical
computation
153         Vel_f(i+1)=1*10^-10; % to avoid spurious numerical error
154         Disp_f(i+1)=Disp_f(i);
155     else
156         Disp_f(i+1)=Disp_f(i)+delta_t*Vel_f(i)+(0.5-beta)*delta_t^2*Acc_f(i)+beta*
delta_t^2*Acc_f(i+1);
157     end
158 else
159     break
160 end
161 end

```

References

- Adachi, K., Yoshioka, N., 1973. On creeping flow of a visco-plastic fluid past a circular cylinder. *Chem. Eng. Sci.* 28 (1), 215–226.
- Ancey, C., 2007. Plasticity and geophysical flows: a review. *J. Non-Newton. Fluid Mech.* 142 (1–3), 4–35.
- API, 2004. Specification for line pipe. Technical Report, American Petroleum Institute.
- Bai, Q., Bai, Y., 2014. *Subsea Pipeline Design, Analysis, and Installation*. Gulf Professional Publishing.
- Bransby, M., Newson, T., Brunning, P., 2002. The upheaval capacity of pipelines in jetted clay backfill. *Int. J. Offshore and Polar Eng.* 12 (04).
- Byrne, B., Schupp, J., Martin, C., Maconochie, A., Oliphant, J., Cathie, D., 2013. Uplift of shallowly buried pipe sections in saturated very loose sand. *Géotechnique* 63 (5), 382–390.
- Chen, W.-F., Liu, X., 2012. *Limit Analysis in Soil Mechanics*. Elsevier.
- Cremonesi, M., Ferrara, L., Frangi, A., Perego, U., 2010. Simulation of the flow of fresh cement suspensions by a Lagrangian finite element approach. *J. Non-Newton. Fluid Mech.* 165 (23–24), 1555–1563.
- Cremonesi, M., Franci, A., Idelsohn, S., Oñate, E., 2020. A State of the Art Review of the Particle Finite Element Method (PFEM). *Arch. Comput. Methods Eng.* 27 (5), 1709–1735.
- Cremonesi, M., Frangi, A., Perego, U., 2011. A Lagrangian finite element approach for the simulation of water-waves induced by landslides. *Comput. Struct.* 89 (11–12), 1086–1093.
- Damgaard, J., Palmer, A., 2001. Pipeline stability on a mobile and liquefied seabed: a discussion of magnitudes and engineering implications. In: *OMAE 2001: Proceedings of the 20th International Conference on Offshore Mechanics and Arctic Engineering*, Rio de Janeiro, Brazil, 4, American Society of Mechanical Engineers, pp. 195–204.
- De Besses, B.D., Magnin, A., Jay, P., 2003. Viscoplastic flow around a cylinder in an infinite medium. *J. Non-Newton. Fluid Mech.* 115 (1), 27–49.
- Della Vecchia, G., Cremonesi, M., Pisanò, F., 2019. On the rheological characterisation of liquefied sands through the dam-breaking test. *Int. J. Numer. Anal. Methods Geomech.* 43 (7), 1410–1425.
- DNV, 2021a. Standard DNV-RP-F109 On-bottom stability design of submarine pipelines.
- DNV, 2021b. Standard DNV-RP-F110 Global buckling of submarine pipelines.
- DNV, 2021c. Standard DNV-ST-F101 Submarine pipeline systems.
- Finn, W.L., Bransby, P.L., Pickering, D.J., 1970. Effect of strain history on liquefaction of sand. *J. Soil Mech. Found. Div.* 96 (6), 1917–1934.
- Gallage, C.P.K., Towhata, I., Nishimura, S., 2005. Laboratory investigation on rate-dependent properties of sand undergoing low confining effective stress. *Soils Found.* 45 (4), 43–60.
- de Groot, M.B., Bolton, M.D., Foray, P., Meijers, P., Palmer, A.C., Sandven, R., Sawicki, A., Teh, T.C., 2006. Physics of liquefaction phenomena around marine structures. *J. Waterw. Port Coast. Ocean Eng.* 132 (4), 227–243.
- Guoxing, C., Enquan, Z., Zhihua, W., Binghui, W., Xiaojun, L., 2016. Experimental investigation on fluid characteristics of medium dense saturated fine sand in pre-and post-liquefaction. *Bull. Earthq. Eng.* 14 (8), 2185–2212.
- Hamada, M., Sato, H., Doi, M., 1993. An experimental study of mechanical properties of liquefied soil and large ground displacement. In: *Proceedings of the US Japan Workshop on Site Response and Ground Failures During Earthquakes*, Napa Valley, California, USA.
- Horsten, T., 2016. Pipe uplift in liquefied sands: the case of induced earthquakes in the Groningen area. Master's thesis. Delft University of Technology.
- Hwang, J.I., Kim, C.Y., Chung, C.K., Kim, M.M., 2006. Viscous fluid characteristics of liquefied soils and behavior of piles subjected to flow of liquefied soils. *Soil Dyn. Earthq. Eng.* 26 (2–4 SPEC. ISS.), 313–323.
- Idelsohn, S.R., Oñate, E., Pin, F.D., 2004. The particle finite element method: a powerful tool to solve incompressible flows with free-surfaces and breaking waves. *Internat. J. Numer. Methods Engrg.* 61 (7), 964–989.
- IEA, 2018. *World Energy Outlook: Offshore Energy Outlook*. Technical Report, International Energy Agency.
- Ishihara, K., 1993. Liquefaction and flow failure during earthquakes. *Géotechnique* 43 (3), 351–451.
- Ishihara, K., Okada, S., 1978. Effects of stress history on cyclic behavior of sand. *Soils Found.* 18 (4), 31–45.
- ISO, 2012. ISO-3183: Petroleum and natural gas industries — Steel pipe for pipeline transportation systems. Technical Report, International Organization for Standardization.
- Jossic, L., Magnin, A., 2009. Drag of an isolated cylinder and interactions between two cylinders in yield stress fluids. *J. Non-Newton. Fluid Mech.* 164 (1–3), 9–16.
- Kang, Z., Zhang, S., 1980. A preliminary analysis of the characteristics of debris flow. In: *Proceedings of the International Symposium on River Sedimentation*. Chinese Society for Hydraulic Engineering Beijing, pp. 225–226.
- Kawakami, T., Suemasa, N., Hamada, H., Sato, H., Katada, T., 1994. Experimental study on mechanical properties of liquefied sand. In: *Proceedings from the Fifth US-Japan Workshop on Earthquake Resistant Design of Lifeline Facilities and Countermeasures Against Soil Liquefaction*. pp. 285–298.
- Lamb, H., 1911. On the uniform motion of a sphere through a viscous fluid. *Philos. Mag. J. Sci.*
- Luan, M., Qu, P., Jeng, D.-S., Guo, Y., Yang, Q., 2008. Dynamic response of a porous seabed-pipeline interaction under wave loading: soil-pipeline contact effects and inertial effects. *Comput. Geotech.* 35 (2), 173–186.
- Major, J.J., Pierson, T.C., 1992. Debris flow rheology: Experimental analysis of fine-grained slurries. *Water Resour. Res.* 28 (3), 841–857.
- Marveggio, P., Redaelli, I., di Prisco, C., 2021. A new constitutive approach for simulating solid-to fluid-like phase transition in dry and saturated granular media. In: *International Conference of the International Association for Computer Methods and Advances in Geomechanics*. Springer, pp. 491–497.
- Mitsoulis, E., 2004. On creeping drag flow of a viscoplastic fluid past a circular cylinder: Wall effects. *Chem. Eng. Sci.* 59 (4), 789–800.
- Miyamoto, J., Sassa, S., Tsurugasaki, K., Sumida, H., 2020. Wave-induced liquefaction and floatation of a pipeline in a drum centrifuge. *J. Waterw. Port Coast. Ocean Eng.* 146 (2), 04019039.
- Montassar, S., de Buhan, P., 2013. Numerical prediction of liquefied ground characteristics from back-analysis of lateral spreading centrifuge experiments. *Comput. Geotech.* 52, 7–15.
- Moraci, N., Mandaglio, M.C., Gioffre, D., Pitasi, A., 2017. Debris flow susceptibility zoning: an approach applied to a study area. *Italian Geotech. J.* 51 (2), 47–62.
- Newmark, N.M., 1959. A method of computation for structural dynamics. *J. Eng. Mech. Div.* 85 (3), 67–94.
- Nirmalkar, N., Chhabra, R.P., Poole, R.J., 2012. On creeping flow of a Bingham plastic fluid past a square cylinder. *J. Non-Newton. Fluid Mech.* 171–172, 17–30.
- Nishimura, S., Towhata, I., Honda, T., 2002. Laboratory shear tests on viscous nature of liquefied sand. *Soils Found.* 42 (4), 89–98.
- Olson, S.M., Stark, T.D., 2002. Liquefied strength ratio from liquefaction flow failure case histories. *Can. Geotech. J.* 39 (3), 629–647.
- Oseen, C.W., 1910. Über die Stokes'sche Formel und über eine verwandte Aufgabe in der Hydrodynamik. *Arkiv Mat., Astron. Och Fysik* 6, 1.

- Parsons, J.D., Whipple, K.X., Simoni, A., 2001. Experimental study of the grain-flow, fluid-mud transition in debris flows. *J. Geol.* 109 (4), 427–447.
- Pierson, T.C., 2005. Hyperconcentrated flow—transitional process between water flow and debris flow. In: *Debris-Flow Hazards and Related Phenomena*. Springer, pp. 159–202.
- Pipeline Flotation Research Council, 1966. ASCE preliminary research on pipeline flotation. *J. Pipeline Div.* 92 (1), 27–74.
- Pisanò, F., Cremonesi, M., Cecinato, F., Della Vecchia, G., 2020. CFD-based framework for analysis of soil–Pipeline interaction in reconsolidating liquefied sand. *J. Eng. Mech.* 146 (10), 04020119.
- Poulos, S.J., 1981. The steady state of deformation. *J. Geotech. Eng. Div.* 107 (5), 553–562.
- Poulos, S.J., Castro, G., France, J.W., 1985. Liquefaction evaluation procedure. *J. Geotech. Eng.* 111 (6), 772–792.
- Randolph, M.F., Houlsby, G., 1984. The limiting pressure on a circular pile loaded laterally in cohesive soil. *Géotechnique* 34 (4), 613–623.
- Schmertmann, J.H., 1978. Guidelines for cone penetration test: performance and design. Technical Report, United States. Federal Highway Administration.
- Schupp, J., Byrne, B., Eacott, N., Martin, C., Oliphant, J., Maconochie, A., Cathie, D., 2006. Pipeline unburial behaviour in loose sand. In: *International Conference on Offshore Mechanics and Arctic Engineering*. 47497, pp. 297–308.
- Sloan, S., 2013. Geotechnical stability analysis. *Géotechnique* 63 (7), 531–571.
- Stark, T.D., Mesri, G., 1992. Undrained shear strength of liquefied sands for stability analysis. *J. Geotech. Eng.* 118, 1727.
- Sumer, B.M., Fredsøe, J., Christensen, S., Lind, M.T., 1999. Sinking/floatation of pipelines and other objects in liquefied soil under waves. *Coast. Eng.* 38 (2), 53–90.
- Sumer, B.M., Hatipoglu, F., Fredsøe, J., Hansen, N.O., 2006. Critical flotation density of pipelines in soils liquefied by waves and density of liquefied soils. *J. Waterw. Port Coast. Ocean Eng.* 132 (4), 252–265.
- Takaisi, Y., 1956. Note on the drag on a circular cylinder moving with low speeds in a viscous liquid between two parallel walls. *J. Phys. Soc. Japan* 11 (9), 1009–1013.
- Tamate, S., Towhata, I., 1999. Numerical simulation of ground flow caused by seismic liquefaction. *Soil Dyn. Earthq. Eng.* 18 (7), 473–485.
- Teh, T., Palmer, A., Bolton, M., Damgaard, J., 2006. Stability of submarine pipelines on liquefied seabeds. *J. Waterw. Port Coast. Ocean Eng.* 132 (4), 244–251.
- Tokpavi, D.L., Magnin, A., Jay, P., 2008. Very slow flow of Bingham viscoplastic fluid around a circular cylinder. *J. Non-Newton. Fluid Mech.* 154 (1), 65–76.
- Tomotika, S., Aoi, T., 1951. An expansion formula for the drag on a circular cylinder moving through a viscous fluid at small Reynolds numbers. *Quart. J. Mech. Appl. Math.* 4 (4), 401–406.
- Towhata, I., Anh, T.T.L., Motamed, R., Sesov, V., 2009. Rate dependent nature of liquefied sand undergoing large flow deformation and its interaction with group pile foundation. In: *The Nineteenth International Offshore and Polar Engineering Conference*. OnePetro.
- Towhata, I., Vargas-Monge, W., Orense, R., Yao, M., 1999. Shaking table tests on subgrade reaction of pipe embedded in sandy liquefied subsoil. *Soil Dyn. Earthq. Eng.* 18 (5), 347–361.
- Uzuoka, R., Yashima, A., Kawakami, T., Konrad, J.-M., 1998. Fluid dynamics based prediction of liquefaction induced lateral spreading. *Comput. Geotech.* 22 (3–4), 243–282.
- Vaid, Y., Thomas, J., 1995. Liquefaction and postliquefaction behavior of sand. *J. Geotech. Eng.* 121 (2), 163–173.
- Vescovi, D., Redaelli, I., di Prisco, C., 2020. Modelling phase transition in granular materials: from discontinuum to continuum. *Int. J. Solids Struct.* 202, 495–510.
- White, C., 1946. The drag of cylinders in fluids at slow speeds. *Proc. R. Soc. Lond. Ser. A Math. Phys. Sci.* 186 (1007), 472–479.
- Wood, D.M., 1990. *Soil Behaviour and Critical State Soil Mechanics*. Cambridge University Press.
- Zdravkovich, M.M., 1979. A critical remark on use of drag coefficient at low Reynolds number. *Zb. Rad.* (11), 152–156.